
EXPLORING THE ROLE OF POLARIZATION IN FIBER-BASED QUANTUM SOURCES

Carla M. Brunner

Max Planck Institute for the Science of Light,
Staudtstr. 2, 91058 Erlangen, Germany

Friedrich-Alexander-University Erlangen-Nürnberg,
Staudtstr. 7, 91058 Erlangen, Germany

carla.brunner@mpl.mpg.de

Nicolas Y. Joly

Friedrich-Alexander-University Erlangen-Nürnberg,
Staudtstr. 7, 91058 Erlangen, Germany

Max Planck Institute for the Science of Light,
Staudtstr. 2, 91058 Erlangen, Germany

nicolas.joly@mpl.mpg.de

October 17, 2024

ABSTRACT

Optical fibers constitute an attractive platform for the realization of nonlinear and quantum optics processes. Here we show, through theoretical considerations, how polarization effects of both third-order parametric down-conversion and four-wave-mixing in optical fibers may be exploited to enhance detection schemes. We apply our general framework specifically to the case of tapered fibers for photon triplet generation, a long-standing goal within quantum optics, and obtain explicit expectation values for its efficiency. A quantitative investigation of four-wave-mixing in a microstructured solid-core fiber provides significant consequences for the role of polarization in experimental design.

Keywords Photon triplet generation · Microstructured optical fibers · Fiber-based quantum sources

1 Introduction

Over recent decades, we have been witness to not only consequential advancements in both the production and characterization of microstructured optical fibers [1, 2] but also in the area of quantum communication, which frequently builds on accessible sources of entangled photons [3]. Specialty fibers may be employed for the generation of photon pairs or even photon triplets through nonlinear interactions [4, 5]. Several qualities make them a compelling tool for these applications, including the tight confinement of the interacting fields and long interaction lengths [6]. Over the last decades, they have been developed into an incredibly versatile range of various shapes and forms, for example photonic-crystal fibers (PCF), gas- or liquid- filled hollow-core fibers (HCF), twisted fibers, as well as microstructured nano- or tapered fibers [7, 8, 9, 10]. They can serve as implementations of photon-pair generation or twin-beam generation [11] through the process of four-wave-mixing (FWM) and have been proposed as a possible technique to enable photon triplet generation through third-order parametric down-conversion (TOPDC) [12].

Both FWM and TOPDC rely on the third-order nonlinearity of the interaction medium and require fulfillment of the respective phase matching condition. While building wavelength tunable fiber-based photon-pair sources has been achieved, triplet generation through TOPDC in the visible domain remains a long-standing goal within quantum optics. The generation of nonclassical states of light, especially higher-order entanglement, is expected to have far-reaching implications for tests of fundamental quantum mechanics [13], quantum communication [14, 15] and quantum computing [16]. Three-photon state generation has been successfully implemented in the microwave domain [17]. In the visible region, there have been advances in the direction of triplet generation using varying experimental setups, for example depending on cascaded down-conversion processes in nonlinear crystals [18, 19], showing cubic optical parametric down-conversion in a crystal [20], building a triplet source on the basis of quantum dot molecules [21], designing integrated waveguides [22] or hybrid PCFs [23] optimized for TOSPDC.

A promising platform for an implementation of direct TOSPDC is given by tapered optical fibers [24, 12]. The

experimental proposal assumes a standard silica fiber that is tapered down to an outer diameter of just 790.36 nm and pumped by a narrowband laser at 532 nm. Intermodal phase matching is then expected between the higher-order HE_{12} pump mode and the fundamental HE_{11} signal mode at 1596 nm. An adiabatic taper transition is required in order to keep the higher-order pump mode throughout the fiber waist. An experimental realization has to this date been prohibited by the extremely low conversion efficiency.

The strength of nonlinear interactions in optical fibers is commonly described by an effective area A_{eff} , related to the modal overlap of interacting fields [25] and can be derived from overlap integrals [26]. Typically, descriptions involve only a single linear polarization. However, to successfully implement systems that use optical fibers to give rise to nonlinear and quantum processes such as FWM and TOPDC, it is unquestionably valuable to be able to theoretically describe all important aspects, particularly including different polarization states. This can in turn lead to the ability to optimize experiments and detection settings. Here we present an approach that we have developed in the context of triplet generation in tapered optical fibers. We will show that it can similarly be used to explain effects that pertain to seeded TOPDC in tapered and FWM in other types of specialty fibers.

We first establish a quantization procedure specifically for the situation of optical fiber modes and apply these expressions to derive polarization-dependent rates of triplet generation. Subsequently, we discuss consequences for optimized detection systems and seeded triplet generation. We conclude by carrying out a quantitative analysis of polarization effects in the FWM case, coinciding with prior studies of classical models of pulse propagation and supercontinuum generation in optical fibers based on the nonlinear Schrödinger equation [27].

2 Quantization of the electromagnetic field in optical fibers

The derivation of a theoretical triplet rate in optical fibers necessitates expressions for quantized optical fiber modes involved in the nonlinear interaction. To that end, we start off with Maxwell's equations and follow a similar quantization procedure for fields in inhomogeneous dielectrics as presented by Milonni [28]. Using the gauge fixing $\Phi = 0$, $\nabla \cdot [\epsilon(\mathbf{r}, \omega)\mathbf{A}] = 0$ for the electric scalar potential Φ and the magnetic vector potential \mathbf{A} , where ϵ is the generally position- and frequency-dependent relative permittivity, a generalization of the Coulomb gauge, the classical vector potential is a solution to the equation of motion

$$\frac{\epsilon(\mathbf{r}, \omega)}{c^2} \frac{\partial^2 \mathbf{A}}{\partial t^2} + \nabla \times (\nabla \times \mathbf{A}) = 0, \quad (1)$$

with t , c denoting time and vacuum speed of light, and can be expanded in a set of spatial vectorial eigenmodes $\mathbf{f}_\xi(\mathbf{r})$,

$$\mathbf{A}(\mathbf{r}, t) = \sum_{\xi} \alpha_{\xi}(t) \mathbf{f}_{\xi}(\mathbf{r}) + \alpha_{\xi}^*(t) \mathbf{f}_{\xi}^*(\mathbf{r}), \quad (2)$$

determined by the solutions of the classical Maxwell equations, where the expansion coefficients $\alpha_{\xi}(t) = \alpha_{\xi}(t_0) e^{-i\omega_{\xi}(t-t_0)}$, $\alpha_{\xi}^*(t) = \alpha_{\xi}^*(t_0) e^{i\omega_{\xi}(t-t_0)}$, for some initial time t_0 , oscillate sinusoidally in time and the subscript ξ runs over the possible solutions of

$$-\frac{\epsilon(\mathbf{r})\omega_{\xi}^2}{c^2} \mathbf{f}_{\xi} + \nabla \times (\nabla \times \mathbf{f}_{\xi}) = 0. \quad (3)$$

Since $\Phi = 0$, the expansion gives rise to the physical electric and magnetic fields as

$$\begin{aligned} \mathbf{E}(\mathbf{r}, t) &= -\nabla\Phi - \frac{\partial \mathbf{A}}{\partial t} = \sum_{\xi} i\omega_{\xi} \alpha_{\xi}(t) \mathbf{f}_{\xi}(\mathbf{r}) - i\omega_{\xi} \alpha_{\xi}^*(t) \mathbf{f}_{\xi}^*(\mathbf{r}), \\ \mathbf{B}(\mathbf{r}, t) &= \nabla \times \mathbf{A} = \sum_{\xi} \alpha_{\xi}(t) (\nabla \times \mathbf{f}_{\xi}(\mathbf{r})) + \alpha_{\xi}^*(t) (\nabla \times \mathbf{f}_{\xi}^*(\mathbf{r})). \end{aligned} \quad (4)$$

Let us now consider a single mode, $\mathbf{A} = \alpha \mathbf{f} + \alpha^* \mathbf{f}^*$. The classical field energy \mathcal{E} is dependent on the material dispersion properties (for a derivation of this expression see suppl. material (SM), eq. S8) reads

$$\mathcal{E} = 2\omega^2 |\alpha|^2 \int_V d^3\mathbf{r} \left[\frac{\frac{d}{d\omega}(\epsilon\omega) + \epsilon}{2} \epsilon_0 |\mathbf{f}|^2 \right] \quad (5)$$

and we choose the normalization

$$\int_V d^3\mathbf{r} \left[\frac{\frac{d}{d\omega}(\epsilon\omega) + \epsilon}{2} \epsilon_0 |\mathbf{f}|^2 \right] = 1. \quad (6)$$

The electromagnetic field energy is equated to the Hamiltonian of a quantum Harmonic Oscillator, $H_{HO} = \frac{1}{2}(p^2 + \omega^2 q^2)$, by writing the canonically conjugate position and momentum variables as $q(t) = i(\alpha(t) - \alpha^*(t))$, $p(t) = \omega(\alpha(t) +$

$\alpha^*(t)$), obeying the Hamiltonian equations of motion. We now replace the classical variables by their quantum counterparts, $\alpha(t) \rightarrow C\hat{a}(t)$, $\alpha^*(t) \rightarrow C^*\hat{a}^\dagger(t)$, with the canonical commutation relations $[\hat{a}_\xi, \hat{a}_{\xi'}^\dagger] = \delta_{\xi\xi'}$. From $[q, p] = i\hbar$ it follows that the constant $C_\xi = \sqrt{\frac{\hbar}{2\omega_\xi}}$. Hence,

$$\begin{aligned}\hat{\mathbf{A}}(\mathbf{r}, t) &= \sum_{\xi} \sqrt{\frac{\hbar}{2\omega_\xi}} \left[\hat{a}_\xi(t) \mathbf{f}_\xi(\mathbf{r}) + \hat{a}_\xi^\dagger(t) \mathbf{f}_\xi^*(\mathbf{r}) \right], \\ \hat{\mathbf{E}}(\mathbf{r}, t) &= i \sum_{\xi} \sqrt{\frac{\hbar\omega_\xi}{2}} \left[\hat{a}_\xi(t) \mathbf{f}_\xi(\mathbf{r}) - \hat{a}_\xi^\dagger(t) \mathbf{f}_\xi^*(\mathbf{r}) \right],\end{aligned}\tag{7}$$

where the first terms correspond to the positive and the second terms to the negative frequency components respectively. In the present case of optical fibers, the eigenmodes \mathbf{f} are related to the mode field components as will be detailed below.

3 The rate of triplet generation

Adopting the expressions of electric field operators in optical fibers, in this section, we derive the triplet generation rate in fibers. To this end, we assume low conversion efficiency so that the rate of triplet rate per signal modes configuration is given by Fermi's Golden Rule [29],

$$\Gamma_{\text{triplet}} = \frac{2\pi}{\hbar^2} \delta(\Delta\omega) |\langle \alpha(N_p - 1), 1, 1, 1 | \hat{H}_I | \alpha(N_p), 0, 0, 0 \rangle|^2,\tag{8}$$

where N_p is the mean pump photon number and \hat{H}_I is the interaction Hamiltonian,

$$\hat{H}_I = -\epsilon_0 \cdot 4 \cdot 3! \cdot \chi_{ijkl}^{(3)} \int_{V_I} d^3\mathbf{r} \hat{E}_{p,i}^{(+)} \hat{E}_{s_1,j}^{(-)} \hat{E}_{s_2,k}^{(-)} \hat{E}_{s_3,l}^{(-)} + \text{h.c.}\tag{9}$$

$\chi^{(3)}$ is the third-order nonlinear susceptibility tensor. Here we assume only a weak dependency on the signal frequencies, i.e. $\chi^{(3)} \equiv \chi^{(3)}(\omega_p; \omega_s, \omega_s, \omega_s)$, and we use Einstein's summation convention to sum over the indices $i, j, k, l = x, y, z$ or $i, j, k, l = r, \phi, z$ in cylindrical coordinates. V_I denotes the interaction volume of a fiber of length L , e.g. the fused silica core in case of a tapered fiber. The initial and final states are $\psi_i = |\alpha(N_p), 0, 0, 0\rangle$ and $\psi_f = |\alpha(N_p - 1), 1, 1, 1\rangle$, where $|\alpha(N)\rangle$ is the coherent pump state with a mean photon number N . The total rate of triplet generation is obtained by summation over all signal mode configurations of the degrees of freedom, including polarization,

$$R_{\text{triplet}} = \sum_{\xi_{s_1}} \sum_{\xi_{s_2}} \sum_{\xi_{s_3}} \frac{2\pi}{\hbar^2} \delta(\Delta\omega) |\langle \hat{H}_I \rangle|^2.\tag{10}$$

Considering the quantized electric field of just a single fiber mode and polarization, a one-to-one relationship between the labels ξ and propagation constants β can be established. The summation is hence written as $\sum_{\xi} \rightarrow \sum_{\sigma} \frac{L}{2\pi} \int d\beta$, since each propagation constant β covers a phase-space volume of $\frac{2\pi}{L}$. Here, σ denotes one of two orthogonal polarization states. Therefore,

$$\begin{aligned}R_{\text{triplet}} &= \sum_{\sigma_{s_1}, \sigma_{s_2}, \sigma_{s_3}} \left(\frac{L}{2\pi} \right)^3 \iiint d\beta_{s_1} d\beta_{s_2} d\beta_{s_3} \frac{2\pi}{\hbar^2} \delta(\Delta\omega) |\langle \hat{H}_I \rangle|^2 \\ &= \sum_{\sigma_{s_1}, \sigma_{s_2}, \sigma_{s_3}} \left(\frac{L}{2\pi} \right)^3 \iiint d\omega_{s_1} d\omega_{s_2} d\omega_{s_3} \left. \frac{d\beta}{d\omega} \right|_{\omega_{s_1}} \left. \frac{d\beta}{d\omega} \right|_{\omega_{s_2}} \left. \frac{d\beta}{d\omega} \right|_{\omega_{s_3}} \frac{2\pi}{\hbar^2} \delta(\Delta\omega) |\langle \hat{H}_I \rangle|^2 \\ &= \sum_{\sigma_{s_1}, \sigma_{s_2}, \sigma_{s_3}} \left(\frac{L}{2\pi} \right)^3 \iint d\omega_{s_1} d\omega_{s_2} \left[\left. \frac{d\beta}{d\omega} \right|_{\omega_{s_1}} \left. \frac{d\beta}{d\omega} \right|_{\omega_{s_2}} \left. \frac{d\beta}{d\omega} \right|_{\omega_{s_3}} \frac{2\pi}{\hbar^2} |\langle \hat{H}_I \rangle|^2 \right]_{\Delta\omega=0}\end{aligned}\tag{11}$$

and a finite detection bandwidth can be taken into account by adjusting the integration limits accordingly. Separating the integrals in the expression for \hat{H}_I (eq. 9) into longitudinal integration over the fiber length L and transversal integration over the fiber cross-section A_I (see SM, eq. S9), \hat{H}_I evaluates to

$$\begin{aligned}\hat{H}_I &= 24\chi_{ijkl}^{(3)} \epsilon_0 \sqrt{\frac{\hbar\omega_p}{2}} \sqrt{\frac{\hbar\omega_{s_1}}{2}} \sqrt{\frac{\hbar\omega_{s_2}}{2}} \sqrt{\frac{\hbar\omega_{s_3}}{2}} a_p a_{s_1}^\dagger a_{s_2}^\dagger a_{s_3}^\dagger \frac{1}{L^2} \frac{1}{\sqrt{M_p M_{s_1} M_{s_2} M_{s_3}}} \\ &\quad \times \int_L dz e^{i(\beta_p - \beta_{s_1} - \beta_{s_2} - \beta_{s_3})z} \int_{A_I} dx dy \mathcal{I}_{ijkl}(x, y) + \text{h.c.}\end{aligned}\tag{12}$$

Here we have used the solutions $\mathbf{e}(x, y)$ for electromagnetic fields of modes propagating in cylindrical step-index fibers as given in [30], for which $\mathbf{e}(x, y)e^{i\beta z}$ are solutions to the wave equation (eq. 3) and introduced

$$\begin{aligned}\mathbf{f} &= \frac{1}{\sqrt{LM}} e^{i\beta z} \mathbf{e}, \\ M &= \int_{A_\infty} dx dy \frac{\frac{d}{d\omega}(\epsilon\omega) + \epsilon}{2} \epsilon_0 \mathbf{e}(x, y) \cdot \mathbf{e}^*(x, y), \\ 1 &= \int_V d^3\mathbf{r} \left[\frac{\frac{d}{d\omega}(\epsilon\omega) + \epsilon}{2} \epsilon_0 |\mathbf{f}|^2 \right] \\ \mathcal{I}_{ijkl}(x, y) &:= e_{p,i}(x, y) e_{s_1,j}^*(x, y) e_{s_2,k}^*(x, y) e_{s_3,l}^*(x, y).\end{aligned}\tag{13}$$

Continuing with the evaluation of the triplet rate, we have

$$\langle \alpha(N_p - 1) | a_p | \alpha(N_p) \rangle \approx \sqrt{N_p}\tag{14}$$

in the limit of large pump photon numbers N_p (see SM, eq. S10) and $\langle 1, 1, 1 | \hat{a}_{s_1}^\dagger \hat{a}_{s_2}^\dagger \hat{a}_{s_3}^\dagger | 0, 0, 0 \rangle = 1$, so that

$$\begin{aligned}|\langle \hat{H}_I \rangle|^2 &= 24^2 N_p \epsilon_0^2 \frac{\hbar^4 \omega_p \omega_{s_1} \omega_{s_2} \omega_{s_3}}{2^4} \frac{1}{L^4} \frac{1}{M_p M_{s_1} M_{s_2} M_{s_3}} \\ &\times \left| \int_L dz e^{i(\beta_p - \beta_{s_1} - \beta_{s_2} - \beta_{s_3})z} \right|^2 \left| \chi_{ijkl}^{(3)} \int_{A_I} dx dy \mathcal{I}_{ijkl}(x, y) \right|^2.\end{aligned}\tag{15}$$

Furthermore, we define the mode overlap as

$$\mathcal{O} = \left| \hat{\chi}_{ijkl}^{(3)} \int_{A_I} dx dy \mathcal{I}_{ijkl}(x, y) \right|^2,\tag{16}$$

where $\hat{\chi}_{ijkl}^{(3)}$ is the normalized third-order nonlinear susceptibility, $\hat{\chi}_{ijkl}^{(3)} := 3\chi_{ijkl}^{(3)}/\chi_{xxxx}^{(3)}$. The phase mismatch factor with wavevector mismatch $\Delta\beta := \beta_p - \beta_{s_1} - \beta_{s_2} - \beta_{s_3}$ evaluates to

$$\left| \int_L dz e^{-i(\beta_p - \beta_{s_1} - \beta_{s_2} - \beta_{s_3})z} \right|^2 = L^2 \text{sinc}^2\left(\frac{\Delta\beta L}{2}\right).\tag{17}$$

Thus,

$$|\langle \hat{H}_I \rangle|^2 = \frac{36 N_p (\chi_{xxxx}^{(3)}/3)^2 \epsilon_0^2 \hbar^4 \omega_p \omega_{s_1} \omega_{s_2} \omega_{s_3}}{L^2 M_p M_{s_1} M_{s_2} M_{s_3}} \text{sinc}^2\left(\frac{\Delta\beta L}{2}\right) \mathcal{O}.\tag{18}$$

Finally, the triplet generation rate becomes

$$\begin{aligned}R_{\text{triplet}} &= \sum_{\sigma_{s_1}, \sigma_{s_2}, \sigma_{s_3}} \frac{P_p L^2 n_p (\chi_{xxxx}^{(3)})^2 \epsilon_0^2 \hbar}{\pi^2 c} \\ &\times \iint d\omega_{s_1} d\omega_{s_2} \left[\frac{\omega_{s_1} \omega_{s_2} \omega_{s_3}}{M_p M_{s_1} M_{s_2} M_{s_3}} \frac{d\beta}{d\omega} \Big|_{\omega_{s_1}} \frac{d\beta}{d\omega} \Big|_{\omega_{s_2}} \frac{d\beta}{d\omega} \Big|_{\omega_{s_3}} \text{sinc}^2\left(\frac{\Delta\beta L}{2}\right) \mathcal{O} \right] \Big|_{\Delta\omega=0}.\end{aligned}\tag{19}$$

Using this result, we are now able to calculate the expected triplet rate for an ideal fiber with the degenerate phase-matching radius of 395.18 nm, a taper waist length of 4 cm and a pump power of 100 mW, assuming $\chi_{xxxx}^{(3)} = 2.8 \times 10^{-22} \text{m}^2/\text{V}^2$. Independent of the pump polarization state, we obtain a total triplet rate of 5.1 Hz. Excitation of the pump mode can be achieved through a number of methods, e.g. by conversion of the fundamental mode via long-period-gratings [31]. We can also draw a conclusion on the polarization state of the generated triplets, as will be discussed in the following section.

3.1 Mode overlap and the role of polarization

While the fiber modes are not plane waves and can therefore not be ascribed a pure polarization state, the even and odd fiber modes are primarily polarized in the two linear orthogonal x, y direction. In the following we will refer to these fiber modes as linearly polarized ($'x', 'y'$) and their complex superpositions as circularly polarized ($'L', 'R'$). We first

consider a linear pump polarization (e.g. x -polarization) and restrict the sum in eq. 19 to different signal polarization configurations in the linear basis. We find that 75% of triplets are generated in the x - x - x polarization configuration (configuration A), 25% in the indistinguishable x - y - y / y - x - y / y - y - x configurations (configuration B), and none in the other configurations. In the case of a circularly polarized pump (e.g. L) and in the circular polarization basis, 100% of triplets are generated in a configuration where one of the signal photons is right circularly polarized (R) and two of the signal photons are left circularly polarized (L) (configuration C). Note that this is a form of angular momentum conservation in the cylindrically symmetric tapered fiber as can be conjectured by Noether's theorem.

To further understand the emergence of angular momentum conservation in our expression, we look into the derived triplet rate in more detail, specifically into the mode overlap \mathcal{O} and the mode overlap integrand $\mathcal{I}_{ijkl} = e_{p,i}e_{s_1,j}^*e_{s_2,k}^*e_{s_3,l}^*$. Firstly, we consider pump and signal photons in the circular polarization basis and assume an L pump. In principle, one possible triplet polarization configuration would be L,L,L. In figure 1, we show several components of the mode overlap integrand with indices in cylindrical coordinates. Evidently, each of these components

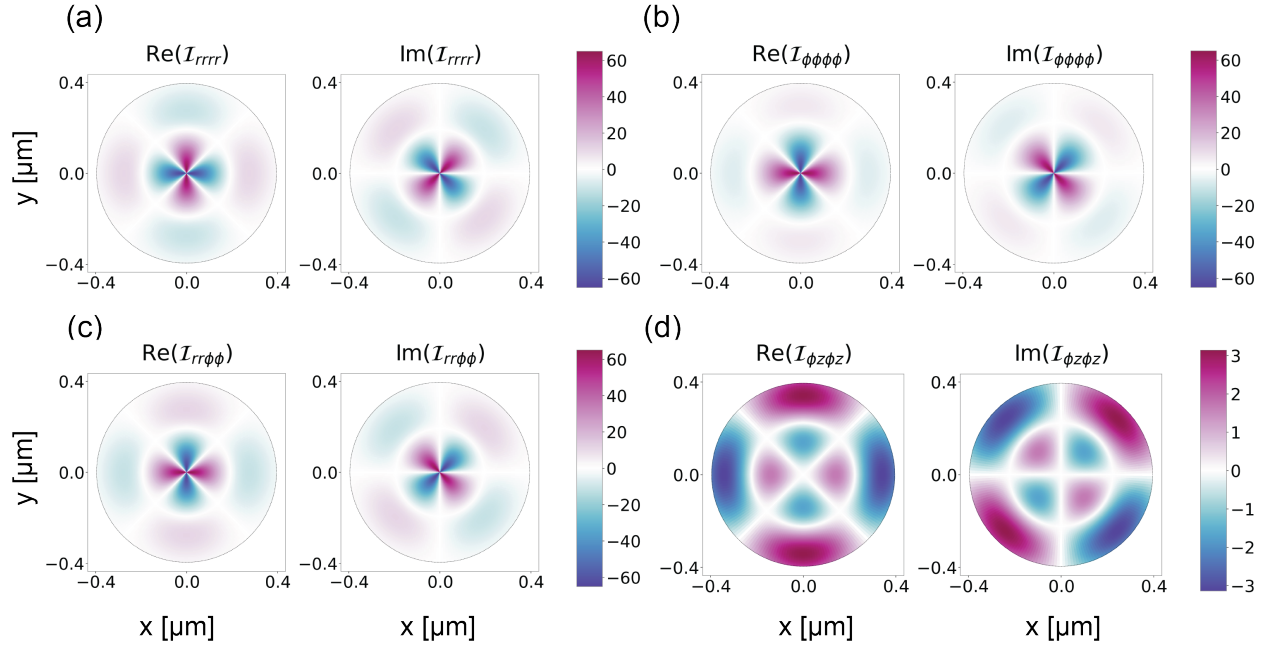


Figure 1: Real and imaginary parts of selected components of the mode overlap integrand \mathcal{I}_{ijkl} for the L \rightarrow L,L,L configuration. The colorbars indicate the magnitudes of $\text{Re}[\mathcal{I}(x, y)]$ and $\text{Im}[\mathcal{I}(x, y)]$ respectively. Integrating the \mathcal{I}_{ijkl} over the interaction area and summation gives a zero mode overlap and thus a zero triplet rate. (a) $\mathcal{I}_{rrrr} = e_{p,r}e_{s_1,r}^*e_{s_2,r}^*e_{s_3,r}^*$, (b) $\mathcal{I}_{\phi\phi\phi\phi} = e_{p,\phi}e_{s_1,\phi}^*e_{s_2,\phi}^*e_{s_3,\phi}^*$, (c) $\mathcal{I}_{rr\phi\phi} = e_{p,r}e_{s_1,r}^*e_{s_2,\phi}^*e_{s_3,\phi}^*$, (d) $\mathcal{I}_{\phi z\phi z} = e_{p,\phi}e_{s_1,z}^*e_{s_2,\phi}^*e_{s_3,z}^*$.

obeys a symmetry between positive and negative values for both the real and imaginary part so that integration over the mode overlap integrand components results in 0. This is similarly true for the other components (see SM, Fig. S1, Fig. S2). Therefore, in the L \rightarrow L,L,L) configuration, the mode overlap and the triplet rate are 0. The same holds for the L \rightarrow L,R,R (and permutations of the right-hand-side, Fig. S3) and L \rightarrow R,R,R configuration (Fig. S4), examples for which are given in the SM - but remarkably not for the L \rightarrow L,L,R configuration, obeying angular momentum conservation (cf. Fig. 2).

3.2 Optimization of the detection scheme

To detect triplets, three superconducting nanowire single-photon detectors can be used to measure photon coincidence rates. The optical detection bandwidth is determined by choosing appropriate chromatic filters in the detection path which also suppress the pump.

Generated photon triplets will lead to identical arrival times at the detectors and thus to a coincidence-rate signal. However, the three triplet photons are not necessarily directed to different detectors. Furthermore, the detectors have a finite timing uncertainty (on the order of 50 ps). We use a coincidence bin of approximately $\tau = 200$ ps. Additionally, they have a quantum efficiency η_q which is close to but smaller than 1.

The main contribution to accidental coincidences is fluorescence; the number of fluorescence photons is proportional to the pump power and fluorescence is emitted into random directions and hence into fiber modes of random polarization.

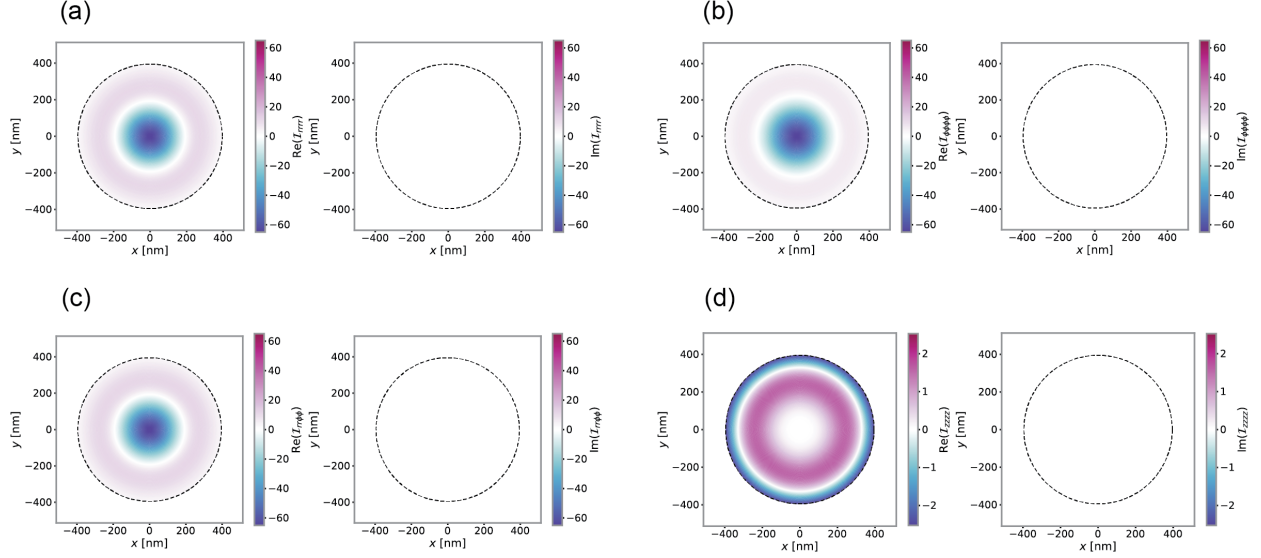


Figure 2: Real and imaginary parts of selected components of the mode overlap integrand \mathcal{I}_{ijkl} for the $L \rightarrow L,L,R$ configuration. The colorbars indicate the magnitudes of $\text{Re}[\mathcal{I}(x, y)]$ and $\text{Im}[\mathcal{I}(x, y)]$ respectively. This configuration obeys angular momentum conservation. The resulting mode overlap and thus triplet rate are nonzero. (a) $\mathcal{I}_{rrrr} = e_{p,r} e_{s_1,r}^* e_{s_2,r}^* e_{s_3,r}^*$, (b) $\mathcal{I}_{\phi\phi\phi\phi} = e_{p,\phi} e_{s_1,\phi}^* e_{s_2,\phi}^* e_{s_3,\phi}^*$, (c) $\mathcal{I}_{rr\phi\phi} = e_{p,r} e_{s_1,r}^* e_{s_2,\phi}^* e_{s_3,\phi}^*$, (d) $\mathcal{I}_{zzzz} = e_{p,z} e_{s_1,z}^* e_{s_2,z}^* e_{s_3,z}^*$.

We aim for the highest coincidence-to-accidental ratio (CAR) [32], given by

$$\text{CAR} = \frac{\text{triplet coincidence detection rate}}{\text{accidental coincidence detection rate}}. \quad (20)$$

The triplet coincidence detection rate is proportional to the triplet rate R_{triplet} but depends on the probabilistic splitting of the signal photons for a specific detection scheme, taking the quantum optical properties of dielectric beamsplitter into account. The accidental coincidence rate due to fluorescence is

$$R_{\text{acc}} = \frac{1}{\tau} (R_{\text{fl}}^{D_1} \tau \eta_q) (R_{\text{fl}}^{D_2} \tau \eta_q) (R_{\text{fl}}^{D_3} \tau \eta_q) = \tau^2 \eta_q^3 R_{\text{fl}}^{D_1} R_{\text{fl}}^{D_2} R_{\text{fl}}^{D_3}, \quad (21)$$

where $R_{\text{fl}}^{D_i}$ denotes the effective fluorescence photon rates at detector i .

3.2.1 Linear pump polarization

The first detection scheme we want to consider is one where the pump is linearly (x -) polarized and only the x - polarized triplet photons are detected (Fig. 3 (a): configuration L). For this purpose, we direct the IR signal onto a polarizing beamsplitter (PBS) to filter out y - polarized photons. Subsequently, we then add a dielectric beamsplitter (BS) and a 50 – 50 BS in one of the detection arms. To determine the optimal BS splitting ration, we need to consider that the general quantum optical description of the state transformation via a lossless BS is given by a unitary operator $U_{BS}(\theta)$,

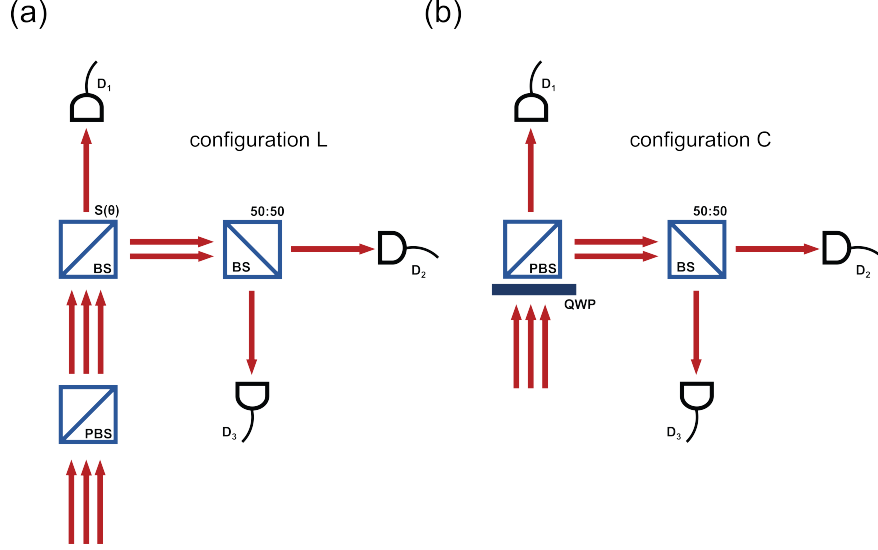


Figure 3: Possible detection schemes for coincidence detection of photon triplets. (a) Linear polarization configuration L ($x \rightarrow x, x, x$) detection. The pump at 532 nm is linearly polarized. The signal IR photons emerging from the fiber, comprising triplet photons and fluorescence (noise) are directed onto a PBS so that only x-polarized photons remain in the detection path. Two additional BS split the triplet photons so that they can be collected by three single-photon detectors D_1, D_2, D_3 . (b) Circular polarization configuration C ($L \rightarrow L, L, R$) detection. A circularly polarized beam serves as pump. The circularly polarized signal IR photons are first transformed to linear polarization states via a QWP. A subsequent PBS separates the previously L-polarized from the R-polarized photons. A BS separates the L-polarized photons so that they impinge on different detectors D_2, D_3 .

$|\text{out}\rangle = U_{BS}(\theta) |\text{in}\rangle$ [33]. The operator acts on an incoming three-photon state as

$$\begin{aligned}
 U_{BS}(\theta) |3, 0\rangle_{\text{in}} &= U_{BS}(\theta) \frac{1}{\sqrt{6}} \left(\hat{a}_1^\dagger \right)^3 |0, 0\rangle_{\text{in}} \\
 &= \frac{1}{\sqrt{6}} \left(\hat{b}_1^\dagger \cos \theta + i \hat{b}_2^\dagger \sin \theta \right)^3 |0, 0\rangle_{\text{out}} \\
 &= \frac{1}{\sqrt{6}} \left[\cos^3 \theta \left(\hat{b}_1^\dagger \right)^3 + 3i \cos^2 \theta \sin \theta \left(\hat{b}_1^\dagger \right)^2 \hat{b}_2^\dagger \right. \\
 &\quad \left. - 3 \cos \theta \sin^2 \theta \hat{b}_1^\dagger \left(\hat{b}_2^\dagger \right)^2 - i \sin^3 \theta \left(\hat{b}_2^\dagger \right)^3 \right] |0, 0\rangle_{\text{out}} \\
 &= \cos^3 \theta |3, 0\rangle_{\text{out}} + \sqrt{3}i \cos^2 \theta \sin \theta |2, 1\rangle_{\text{out}} \\
 &\quad - \sqrt{3} \cos \theta \sin^2 \theta |1, 2\rangle_{\text{out}} - i \sin^3 \theta |0, 3\rangle_{\text{out}},
 \end{aligned} \tag{22}$$

where $\hat{a}_{1,2}^\dagger, \hat{b}_{1,2}^\dagger$ are the photon creation operators of indistinguishable photons of the same polarization at the two inputs and two outputs respectively. A necessary and sufficient condition for triplet coincidence detection is now a two-photon state in the reflection arm, since this two-photon state will deterministically be split into one photon in each arm after the 50 – 50 BS as a result of the Hong-Ou-Mandel effect [34]. The maximum of the associated probability $|\sqrt{3}i \cos^2 \theta \sin \theta|^2$ is obtained for $\sin^2 \theta = \frac{1}{3}$ and thus for a BS with splitting ratio 2 : 1.

In this configuration, a factor of $\frac{4}{9}$ therefore accounts for probabilistic splitting of the triplet photons so that the triplet coincidence detection rate becomes

$$R_{\text{triplet}}^{\text{coinc.}} = \frac{4}{9} \eta_q^3 R_{\text{triplet}}^L, \tag{23}$$

where R_{triplet}^L is the number of triplets per second in the linear configuration L ($x \rightarrow x, x, x$, cf. subsection 3.1).

At the same time, the effective fluorescence photon rates at each detector are equal for D_1, D_2, D_3 , $R_{\text{fl}}^{D_i} = 1/6 R_{\text{fl}}$ ($i = 1, 2, 3$). It follows that the CAR in this case is

$$\text{CAR} = 96 \cdot \frac{1}{\tau^2 R_{\text{fl}}^3} R_{\text{triplet}}^L. \tag{24}$$

3.2.2 Circular pump polarization

In case of circular pump polarization, 2 of the triplet photons will have the same handedness as the pump whereas one has opposite handedness. Hence, with a combination of a quarter-wave-plate (QWP) and a PBS we can separate the two circular polarizations and add a single 50 – 50 BS in the 2-photon arm (Fig. 3 (b): configuration C). The two indistinguishable photons in the first arm are directed onto two different detectors,

$$R_{\text{triplet}}^{\text{coinc.}} = \eta_q^3 R_{\text{triplet}}^{\text{C}}, \quad (25)$$

but $R_{\text{fl}}^{D_1} = \frac{1}{2} R_{\text{fl}}$, $R_{\text{fl}}^{D_2} = R_{\text{fl}}^{D_3} = \frac{1}{4} R_{\text{fl}}$. Using $R_{\text{triplet}}^{\text{L}}/R_{\text{triplet}}^{\text{C}} \approx 1.33$, the CAR in this case is

$$\text{CAR} = 42.7 \cdot \frac{1}{\tau^2 R_{\text{fl}}^3} R_{\text{triplet}}^{\text{L}}. \quad (26)$$

Considering these scenarios, we can therefore conclude that the optimal configuration for the highest possible CAR is to employ a linearly polarized pump beam combined with detection as in the first detection scheme (Fig. 3(a): configuration L).

3.3 Waist radius fluctuations and detection bandwidth requirements

The fabrication of sub-micron tapered fibers with a nearly constant waist radius along the full tapered fiber length is challenging. While the perfect phase-matching diameter can be tuned without changing the pump wavelength by placement of the fiber in a pressure tunable gas cell [12, 35, 36], this cannot account for fluctuations of the waist radius along $0 \leq z \leq L$. In this section, we consider how these fluctuations affect the expected triplet generation rate. We

model these fluctuations as a waist radius $r(z)$ varying along z and following a Gaussian distribution $p(r) \propto e^{-\frac{(r-\mu_r)^2}{2\sigma_r^2}}$ with a mean value μ_r and standard deviation σ_r , but do not take fluctuation-induced losses e.g. due to scattering into other modes into account. We will determine which detection bandwidth is optimal in terms of detected coincidence counts and CAR, assuming the first detection scheme (Fig. 3 (a)), effectively only collecting photons of the same linear polarization as the pump. This leads to a rate of coincidence counts of $R_{\text{coinc}} = \frac{4}{9} \eta_q^3 R_{\text{triplet}}^{\text{L}}$ where $R_{\text{triplet}}^{\text{L}}$ is the integrated triplet rate of configuration L, weighted according to the distribution $p(r)$.

As expected, closer to the perfect phase matching waist radius (Fig. 4 (c) compared to 4 (a)) or with an increased detection bandwidth B (white arrow in Fig. 4 (a)), more coincidences may be detected. For larger waist radius fluctuations ($\sigma = 2.0$ nm), the bandwidth necessary to obtain the same coincidence detection rate also increases (Fig. 4 (d) compared to 4 (c)). However, large detection bandwidths are detrimental to the CAR, since the fluorescence count rate scales linearly with the detection bandwidth B . Nevertheless, the count rates as calculated here suggest that currently available detection techniques allow for demonstration of the photon triplet state with this setup.

4 Seeded TOPDC

We now turn to the case of seeded TOPDC as opposed to spontaneous TOPDC in a tapered fiber. Here, we can take advantage of the fact that the triplet generation rate can be increased by several orders of magnitude with a weak seed beam coupled to the tapered fiber in addition to the pump beam. More specifically, we again assume a pump beam at a wavelength of 532 nm in the higher-order mode HE_{12} and add a seed beam at 1596 nm in the fundamental HE_{11} mode. The interaction Hamiltonian is the same as for the unseeded case,

$$\hat{H}_I = -\epsilon_0 \cdot 4 \cdot 3 \cdot 2! \cdot \chi_{ijkl}^{(3)} \int_{V_I} d^3\mathbf{r} \hat{E}_{p,i}^{(+)} \hat{E}_{s,j}^{(-)} \hat{E}_{s_1,k}^{(-)} \hat{E}_{s_2,l}^{(-)} + \text{h.c.} \quad (27)$$

The seed field is labeled by \hat{E}_s , whereas the generated signal photons correspond to the fields $\hat{E}_{s_1}, \hat{E}_{s_2}$. The seeded triplet generation rate reads

$$R_{\text{triplet,seeded}} = \sum_{\xi_{s_1}} \sum_{\xi_{s_2}} \frac{2\pi}{\hbar^2} \delta(\Delta\omega) |\langle \hat{H}_I \rangle|^2, \quad (28)$$

where

$$\langle \hat{H}_I \rangle = \langle \alpha(N_p - 1), \alpha(N_s + 1), 1, 1 | \hat{H}_I | \alpha(N_p), \alpha(N_s), 0, 0 \rangle. \quad (29)$$

Initially, both the pump and seed states are coherent states with mean photon numbers N_p, N_s respectively. Since the possible signal modes are closely spaced in β -space, the sum is transformed into an integral,

$$R_{\text{triplet,seeded}} = \sum_{\sigma_{s_1}, \sigma_{s_2}} \left(\frac{L}{2\pi} \right)^2 \int d\omega_{s_1} \left[\frac{d\beta}{d\omega} \Big|_{\omega_{s_1}} \frac{d\beta}{d\omega} \Big|_{\omega_{s_2}} \frac{2\pi}{\hbar^2} |\langle \hat{H}_I \rangle|^2 \right] \Big|_{\Delta\omega=0}. \quad (30)$$

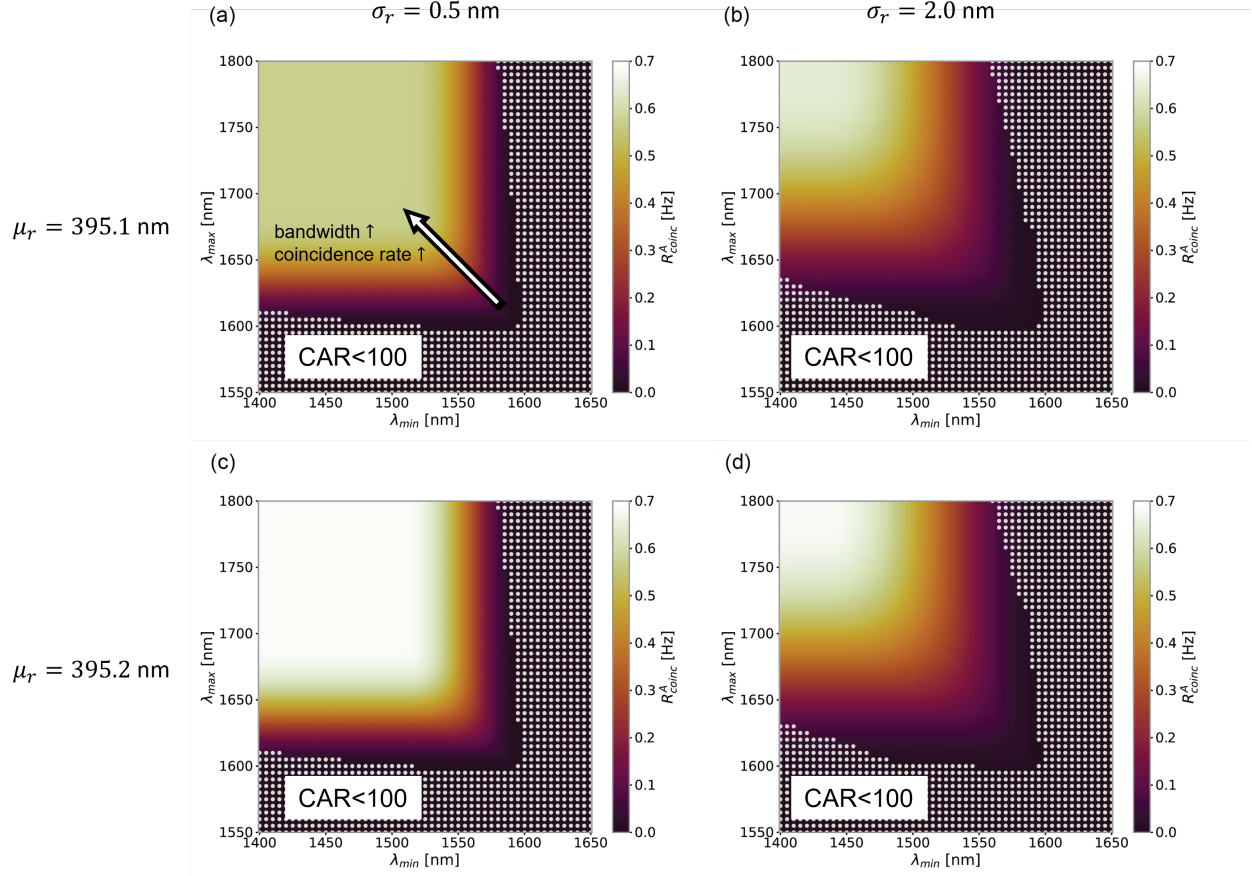


Figure 4: Coincidence rates as obtained for an optical detection bandwidth determined by the detection wavelength limits $\lambda_{min}, \lambda_{max}$ for different Gaussian fiber radius fluctuation distributions centered around μ_r with standard deviation σ_r . The dotted area marks the detection settings where the $CAR < 100$. (a) $\mu_r = 395.1$ nm, $\sigma_r = 0.5$ nm. The white arrow illustrates the increasing coincidence rates as the detection bandwidth grows. (b) $\mu_r = 395.1$ nm, $\sigma_r = 2.0$ nm. (c) $\mu_r = 395.2$ nm, $\sigma_r = 0.5$ nm (d) $\mu_r = 395.2$ nm, $\sigma_r = 2.0$ nm

As discussed in section 3, the integration over the interaction volume in the interaction Hamiltonian can be split up into a longitudinal and transversal component. Furthermore using $\langle \alpha(N_p - 1) | \hat{a}_p | \alpha(N_p) \rangle \approx \sqrt{N_p}$, $\langle \alpha(N_s + 1) | \hat{a}_s^\dagger | \alpha(N_s) \rangle \approx \sqrt{N_s}$, $\langle 1, 1 | \hat{a}_{s_1}^\dagger \hat{a}_{s_2}^\dagger | 0, 0 \rangle = 1$,

$$|\langle \hat{H}_I \rangle|^2 = \frac{36 N_p N_s (\chi_{xxxx}^{(3)})^2 \epsilon_0^2 \hbar^4 \omega_p \omega_s \omega_{s_1} \omega_{s_2}}{L^2 M_p M_s M_{s_1} M_{s_2}} \text{sinc}^2\left(\frac{\Delta\beta L}{2}\right) \mathcal{O}. \quad (31)$$

Note that the mode overlap \mathcal{O} depends on the signal photon polarizations $\sigma_{s_1}, \sigma_{s_2}$. Therefore, the generation rate becomes

$$R_{\text{triplet, seeded}} = \frac{2L^2 P_p P_s n_p n_s (\chi_{xxxx}^{(3)})^2 \epsilon_0^2}{\pi c^2 M_p M_s} \times \sum_{\sigma_{s_1}, \sigma_{s_2}} \int d\omega_{s_1} \left[\frac{\omega_{s_1} \omega_{s_2}}{M_{s_1} M_{s_2}} \frac{d\beta}{d\omega} \Big|_{\omega_{s_1}} \frac{d\beta}{d\omega} \Big|_{\omega_{s_2}} \text{sinc}^2\left(\frac{\Delta\beta L}{2}\right) \mathcal{O} \right] \Big|_{\Delta\omega=0}. \quad (32)$$

We obtain a total seeded triplet generation rate of over 450 000 Hz in the case of perfect phase matching, a taper waist length of 4 cm, $\chi_{xxxx}^{(3)} = 2.8 \times 10^{-22}$ mV, a pump power (x -polarization) of 100 mW and a seed beam (x -polarization) of 40 mW in the higher-order HE_{12} mode. The polarization dependence of the mode overlap is exactly the same as for the unseeded, spontaneous TOPDC case considered above so that polarization settings can be adapted according to the experimental requirements. In terms of detection schemes, we note that not only a coincidence detection scheme can be

used for state characterization. However, the details pertaining to these prospective methods are out of the scope of this paper.

5 Four-Wave-Mixing

Besides an application to TOPDC, a general form of quantized fiber modes of different polarizations lends itself to an analysis of FWM. Polarization effects of FWM or ultrashort pulse propagation in optical fibers have already been theoretically explored for multiple decades [37, 38, 39, 40, 27]. A crucial result was the adherence to angular momentum conservation [37, 39, 41, 27], which restricts the possible pump and signal/idler configurations in FWM. Accurately addressing signal degradation due to Raman scattering in optical fibers, photon pair polarization correlations have been theoretically investigated in [41]. Here, we employ the approach above to gain further quantitative insight into the pure FWM efficiency.

Just as TOPDC, FWM is mediated by the third-order nonlinear susceptibility of the interaction medium. The interaction Hamiltonian can be written as

$$\hat{H}_I = -\epsilon_0 \cdot 4! \cdot \chi_{ijkl}^{(3)} \int_{V_I} d^3\mathbf{r} \hat{E}_{p_1,i}^{(+)} \hat{E}_{p_2,j}^{(+)} \hat{E}_{s_1,k}^{(-)} \hat{E}_{s_2,l}^{(-)} + \text{h.c.}, \quad (33)$$

with $p_1 = p_2 = p$ in the degenerate FWM case. Because of the frequency dependence, $\chi^{(3)} \equiv \chi^{(3)}(\omega_{p_1}, \omega_{p_2}; \omega_{s_1}, \omega_{s_2})$ is generally different from the tensor we previously considered in the context of triplet generation but obeys the same relations between its components in isotropic media. To examine polarization effects in the quasi-CW case, here we need to take the FWM mode overlap into account,

$$\begin{aligned} \mathcal{O}^{\text{FWM}} &= \left| \hat{\chi}_{ijkl}^{(3)} \int_{A_I} dx dy \mathcal{I}_{ijkl}^{\text{FWM}}(x, y) \right|^2, \\ \mathcal{I}_{ijkl}^{\text{FWM}}(x, y) &= e_{p_1,i}(x, y) e_{p_2,j}(x, y) e_{s_1,k}^*(x, y) e_{s_2,l}^*(x, y). \end{aligned} \quad (34)$$

In the low-gain regime, the FWM efficiency is proportional to the mode overlap. Just as for TOPDC, there is negligible signal generation as long as the phase-matching condition is not fulfilled. However, due to the usually large peak intensities used in experiments, this phase-matching condition also contains an additional contribution due to the intensity-dependent refractive index change (AC Kerr-effect), $2\beta_{\text{pump}} = \beta_{\text{signal}} + \beta_{\text{idler}} + 2\gamma P$. It can be realized in the form of intramodal phase matching, for example in solid-core PCF [25, 42]. Solid-core PCF have been shown to provide a bright source for generation of photon pairs [43]. Here, we consider a zero-dispersion-wavelength (ZDW) shifted fiber that is modeled using COMSOL Multiphysics[®] software with an inner silica diameter of 1.5 μm , surrounded by air holes in a honeycomb pattern providing an air filling fraction of 70% as described in [42]. This fiber was experimentally studied in both the normal and anomalous dispersion regime but in the context of tunable optical parametric generation. The obtained ZDW for the simulated fiber is 725 nm. In the normal dispersion regime close to the ZDW, e.g. for a pump wavelength of 722 nm and a power of 1.0 W, the gain is maximal for widely separated sidebands at 634.85 nm and 836.88 nm, following from the phase matching condition.

Figure 5 (a) shows a relative comparison of the obtained mode overlaps for different pump, signal and idler polarizations, directly related to the sideband gain. The electrical field distributions obtained from the simulations have been normalized to equal total intensities, permitting a relative quantitative comparison. Indeed, for configurations that are not angular momentum conserving, there is none or only neglectable gain. We want to emphasize this result since it holds despite the considered PCF structure not perfectly obeying cylindrical symmetry.

In accordance with [39] and contrary to the case of TOPDC, the total gain is not independent of pump polarization but significantly lower for a circularly polarized pump (III). The $x, x \rightarrow y, y$ configuration mode overlap (II) is almost 90% smaller than the one we obtain in the $x, x \rightarrow x, x$ configuration (I). In practice, as mentioned, a main degradation source of the obtained correlation of generated pairs is spontaneous Raman scattering (spRS) [41]. The degenerate pump setting requires co-polarization of the pump fields, so that spRS can only be sufficiently suppressed if the signal and idler are cross-polarized to the pump (case II; not for cases I or III). While configuration I is therefore favorable in the case of widely separated sidebands at hand, configuration II is beneficial for small detuning, a result matching the detailed calculations involving spRS in [41].

On the other hand, the same PCF structure could potentially provide a source of frequency-degenerate photons at 722 nm when pumping at 634 nm and 836 nm, assuming a power of 500 mW at each of the pump frequencies. Then, the pump beams need not be co-polarized. Again, the pair generation rate is linearly related to the mode overlap pertaining to a specific set of polarizations. Fig. 5 (b) summarizes the results we obtain in this case. In case of large frequency detuning and low spRS-induced correlation degradation, the linear polarization configuration IV proves advantageous over the circular polarization configuration V. However, as pointed out in [41], if the pump and signal detuning is within the Raman gain bandwidth, the circular polarization configuration VII is superior over VI because of a higher mode

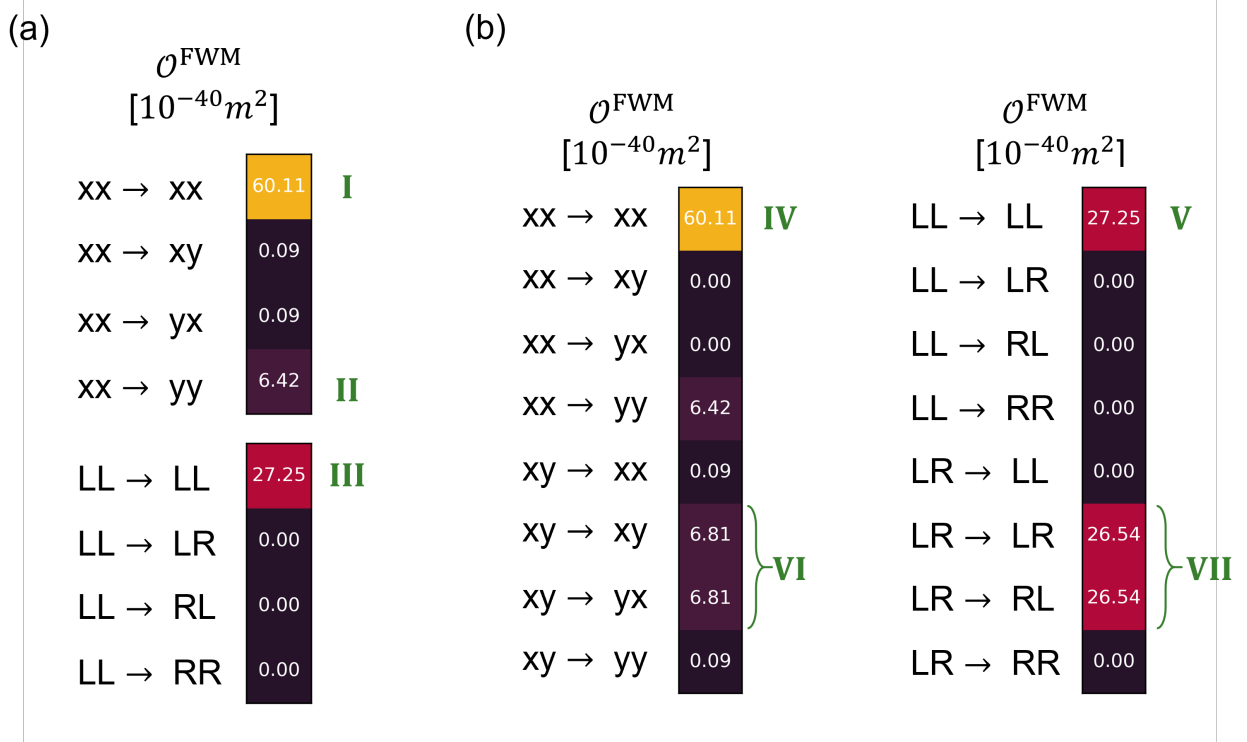


Figure 5: Mode overlap for FWM in the solid-core PCF described above, comparing different pump- and signal-polarization configurations. (a) Linear and circular polarization for a degenerate pump at 722 nm in the normal dispersion regime. Signal and idler can be generated via FWM at 634 nm and 836 nm. While FWM in the $x,x \rightarrow x,x$ configuration is most efficient, pair generation is also expected to be non-negligible in both the $x,x \rightarrow y,y$ and $L,L \rightarrow L,L$ configuration. Note that for circular polarizations, only angular momentum conserving FWM processes are allowed. (b) Linear or circular pump polarization for two non-degenerate pump beams at 634 nm and 836 nm. Signal and idler photon pairs of degenerate wavelength may be generated at 722 nm. While the $x,x \rightarrow x,x$ configuration exhibits the highest mode overlap and therefore nonlinear gain, photon pairs can also be expected in the $x,x \rightarrow y,y$, the $x,y \rightarrow x,y$, the $L,L \rightarrow L,L$ and the $L,R \rightarrow L,R$ configurations.

overlap and superior over IV due to suppression of spRS-induced noise.

Highlighting that configurations II and VII only benefit the correlation signal if spRS plays a significant role, linear co-polarized signal, idler and pump beams (I, IV) always provide an enhanced mode overlap \mathcal{O}^{FWM} . Owing to advances in the manufacturing of noble gas-filled hollow-core fibers [44] with high nonlinearity [45] and findings of large sideband separation in ZDW-shifted PCF, these polarization configurations are expected to be more suitable for a realization of enhanced fiber-based pair generation sources, spectroscopy or imaging with undetected photons [46] or single-photon frequency shifting [47].

6 Conclusion

Starting with a general expression for quantized electromagnetic fields in optical fibers, we have investigated the role of polarization in TOPDC and FWM using a full tensor description of these third-order nonlinear processes. We found that the relative efficiencies are primarily governed by the mode overlap, which is strongly dependent on polarization states. We could predict polarization correlations of triplet photons in TOPDC as well as signal and idler photons in FWM. The analysis has enabled us to optimize the detection scheme for photon triplet states regarding to the signal-to-noise ratio and calculate concrete expected triplet rates. Consequences for ideal experimental design of fiber-based FWM processes are obtained by a quantitative analysis of the mode overlap in FWM involving different polarization configurations.

Funding

The authors acknowledge the Deutsche Forschungsgemeinschaft (DFG, German Research Foundation - JO 1090/3-2) and the International Max Planck Research School Physics of Light (IMPRS-PL) for financial support.

Acknowledgments

The authors thank Maria V. Chekhova for constructive scientific discussions about this work.

Disclosures

The authors declare no conflicts of interest.

Data availability

The authors confirm that the theoretical derivations supporting the findings of this study are available within the article and its supplementary materials. The data and numerical analysis is available from the corresponding authors, upon reasonable request.

References

- [1] M.N. Petrovich, A. van Brakel, F. Poletti, K. Mukasa, E. Austin, V. Finazzi, P. Petropoulos, E. O’Driscoll, M. Watson, T. DelMonte, T.M. Monro, J.P. Dakin, and D.J. Richardson. Microstructured fibers for sensing applications. *Proc. SPIE, Photonic Crystals and Photonic Crystal Fibers for Sensing Applications*, 6005:60050E, November 2005.
- [2] Huanhuan Liu, Dora Juan Juan Hu, Qizhen Sun, Lei Wei, Kaiwei Li, Changrui Liao, Bozhe Li, Cong Zhao, Xinyong Dong, Yuhan Tang, Yihong Xiao, Gerd Keiser, and Perry Ping Shum. Specialty optical fibers for advanced sensing applications. *Opto-Electronic Science*, 2(2):220025–220025, 2023.
- [3] Emma Brambila, Rodrigo Gómez, Riza Fazili, Markus Gräfe, and Fabian Steinlechner. Ultrabright polarization-entangled photon pair source for frequency-multiplexed quantum communication in free-space. *Optics Express*, 31(10):16107, April 2023.
- [4] Karina Garay-Palmett, Dong Beom Kim, Yujie Zhang, Francisco A. Domínguez-Serna, Virginia O. Lorenz, and Alfred B. U’Ren. Fiber-based photon-pair generation: tutorial. *Journal of the Optical Society of America B*, 40(3):469, February 2023.
- [5] A. A. Shukhin, J. Keloth, K. Hakuta, and A. A. Kalachev. Heralded single-photon and correlated-photon-pair generation via spontaneous four-wave mixing in tapered optical fibers. *Phys. Rev. A*, 101:053822, May 2020.
- [6] Cameron McGarry, Kerriane Harrington, Alex O. C. Davis, Peter J. Mosley, and Kristina R. Rusimova. Microstructured optical fibers for quantum applications: Perspective. *APL Quantum*, 1(3):030901, 07 2024.
- [7] T. A. Birks, J. C. Knight, and P. St. J. Russell. Endlessly single-mode photonic crystal fiber. *Optics Letters*, 22(13):961, July 1997.
- [8] J. C. Knight, T. A. Birks, P. St. J. Russell, and J. P. de Sandro. Properties of photonic crystal fiber and the effective index model. *Journal of the Optical Society of America A*, 15(3):748, March 1998.

- [9] Christos Markos, John C. Travers, Amir Abdolvand, Benjamin J. Eggleton, and Ole Bang. Hybrid photonic-crystal fiber. *Rev. Mod. Phys.*, 89:045003, Nov 2017.
- [10] Victor Grubsky and Jack Feinberg. Phase-matched third-harmonic uv generation using low-order modes in a glass micro-fiber. *Optics Communications*, 274(2):447–450, June 2007.
- [11] Martin A. Finger, Timur Sh. Iskhakov, Nicolas Y. Joly, Maria V. Chekhova, and Philip St. J. Russell. Raman-free, noble-gas-filled photonic-crystal fiber source for ultrafast, very bright twin-beam squeezed vacuum. *Phys. Rev. Lett.*, 115:143602, Sep 2015.
- [12] Andrea Cavanna, Jonas Hammer, Cameron Okoth, Erasto Ortiz-Ricardo, Hector Cruz-Ramirez, Karina Garay-Palmett, Alfred B. U'Ren, Michael H. Frosz, Xin Jiang, Nicolas Y. Joly, and Maria V. Chekhova. Progress toward third-order parametric down-conversion in optical fibers. *Phys. Rev. A*, 101:033840, Mar 2020.
- [13] Konrad Banaszek and Peter L. Knight. Quantum interference in three-photon down-conversion. *Physical Review A*, 55(3):2368–2375, March 1997.
- [14] Nicolas Gisin and Rob Thew. Quantum communication. *Nature Photonics*, 1(3):165–171, March 2007.
- [15] Hoi-Kwong Lo, Marcos Curty, and Kiyoshi Tamaki. Secure quantum key distribution. *Nature Photonics*, 8(8):595–604, July 2014.
- [16] Daniel E. Browne and Terry Rudolph. Resource-efficient linear optical quantum computation. *Phys. Rev. Lett.*, 95:010501, Jun 2005.
- [17] C. W. Sandbo Chang, Carlos Sabín, P. Forn-Díaz, Fernando Quijandría, A. M. Vadiraj, I. Nsanzeza, G. Johansson, and C. M. Wilson. Observation of three-photon spontaneous parametric down-conversion in a superconducting parametric cavity. *Phys. Rev. X*, 10:011011, Jan 2020.
- [18] Hannes Hübel, Deny R. Hamel, Alessandro Fedrizzi, Sven Ramelow, Kevin J. Resch, and Thomas Jennewein. Direct generation of photon triplets using cascaded photon-pair sources. *Nature*, 466(7306):601–603, July 2010.
- [19] Deny R. Hamel, Lynden K. Shalm, Hannes Hübel, Aaron J. Miller, Francesco Marsili, Varun B. Verma, Richard P. Mirin, Sae Woo Nam, Kevin J. Resch, and Thomas Jennewein. Direct generation of three-photon polarization entanglement. *Nature Photonics*, 8(10):801–807, September 2014.
- [20] J. Douady and B. Boulanger. Experimental demonstration of a pure third-order optical parametric downconversion process. *Optics Letters*, 29(23):2794, December 2004.
- [21] Milad Khoshnegar, Tobias Huber, Ana Predojević, Dan Dalacu, Maximilian Prilmüller, Jean Lapointe, Xiaohua Wu, Philippe Tamarat, Brahim Lounis, Philip Poole, Gregor Weihs, and Hamed Majedi. A solid state source of photon triplets based on quantum dot molecules. *Nature Communications*, 8(1):15716, June 2017.
- [22] Michael G. Moebius, Felipe Herrera, Sarah Griesse-Nascimento, Orad Reshef, Christopher C. Evans, Gian Giacomo Guerreschi, Alán Aspuru-Guzik, and Eric Mazur. Efficient photon triplet generation in integrated nanophotonic waveguides. *Optics Express*, 24(9):9932, April 2016.
- [23] Andrea Cavanna, Felix Just, Xin Jiang, Gerd Leuchs, Maria V. Chekhova, Philip St. J. Russell, and Nicolas Y. Joly. Hybrid photonic-crystal fiber for single-mode phase matched generation of third harmonic and photon triplets. *Optica*, 3(9):952, August 2016.
- [24] María Corona, Karina Garay-Palmett, and Alfred B. U'Ren. Third-order spontaneous parametric down-conversion in thin optical fibers as a photon-triplet source. *Phys. Rev. A*, 84:033823, Sep 2011.
- [25] W. J. Wadsworth, N. Joly, J. C. Knight, T. A. Birks, F. Biancalana, and P. St. J. Russell. Supercontinuum and four-wave mixing with q-switched pulses in endlessly single-mode photonic crystal fibres. *Optics Express*, 12(2):299, 2004.
- [26] R. Stolen and J. Bjorkholm. Parametric amplification and frequency conversion in optical fibers. *IEEE Journal of Quantum Electronics*, 18(7):1062–1072, July 1982.
- [27] Francesco Poletti and Peter Horak. Description of ultrashort pulse propagation in multimode optical fibers. *Journal of the Optical Society of America B*, 25(10):1645, September 2008.
- [28] Peter W. Milonni. Quantum theory of the electromagnetic field. In *An Introduction to Quantum Optics and Quantum Fluctuations*, pages 129–204. Oxford University Press Oxford, January 2019.
- [29] Cameron Okoth, Andrea Cavanna, Nicolas Y. Joly, and Maria V. Chekhova. Seeded and unseeded high-order parametric down-conversion. *Phys. Rev. A*, 99:043809, Apr 2019.
- [30] Allan W. Snyder and John D. Love. *Optical Waveguide Theory*. Springer US, 1984.
- [31] Yunhe Zhao, Yunqi Liu, Liang Zhang, Chenyi Zhang, Jianxiang Wen, and Tingyun Wang. Mode converter based on the long-period fiber gratings written in the two-mode fiber. *Optics Express*, 24(6):6186, March 2016.

- [32] Marcelo Davanço, Jun Rong Ong, Andrea Bahgat Shehata, Alberto Tosi, Imad Agha, Solomon Assefa, Fengnian Xia, William M. J. Green, Shayan Mookherjea, and Kartik Srinivasan. Telecommunications-band heralded single photons from a silicon nanophotonic chip. *Applied Physics Letters*, 100(26):261104, 06 2012.
- [33] Leonard Mandel and Emil Wolf. *Optical Coherence and Quantum Optics*. Cambridge University Press, September 1995.
- [34] C. K. Hong, Z. Y. Ou, and L. Mandel. Measurement of subpicosecond time intervals between two photons by interference. *Physical Review Letters*, 59(18):2044–2046, November 1987.
- [35] Jonas Hammer, Andrea Cavanna, Riccardo Pennetta, Maria V. Chekhova, Philip St.J. Russell, and Nicolas Y. Joly. Dispersion tuning in sub-micron tapers for third-harmonic and photon triplet generation. *Optics Letters*, 43(10):2320, May 2018.
- [36] Jonas Hammer, Maria V. Chekhova, Daniel R. Häupl, Riccardo Pennetta, and Nicolas Y. Joly. Broadly tunable photon-pair generation in a suspended-core fiber. *Phys. Rev. Res.*, 2:012079, Mar 2020.
- [37] A.L. Berkhoer and V.E. Zakharov. Self excitation of waves with different polarizations in nonlinear media. *Soviet Journal of Experimental and Theoretical Physics*, 31(3):486, January 1970.
- [38] Qiang Lin and Govind P. Agrawal. Vector theory of four-wave mixing: polarization effects in fiber-optic parametric amplifiers. *Journal of the Optical Society of America B*, 21(6):1216, June 2004.
- [39] K. Garay-Palmett, H. J. McGuinness, Offir Cohen, J. S. Lundeen, R. Rangel-Rojo, A. B. U'ren, M. G. Raymer, C. J. McKinstrie, S. Radic, and I. A. Walmsley. Photon pair-state preparation with tailored spectral properties by spontaneous four-wave mixing in photonic-crystal fiber. *Optics Express*, 15(22):14870, 2007.
- [40] C. J McKinstrie and S. Radic. Phase-sensitive amplification in a fiber. *Optics Express*, 12(20):4973, 2004.
- [41] Q. Lin, F. Yaman, and Govind P. Agrawal. Photon-pair generation in optical fibers through four-wave mixing: Role of raman scattering and pump polarization. *Phys. Rev. A*, 75:023803, Feb 2007.
- [42] G. K. L. Wong, A. Y. H. Chen, S. G. Murdoch, R. Leonhardt, J. D. Harvey, N. Y. Joly, J. C. Knight, W. J. Wadsworth, and P. St. J. Russell. Continuous-wave tunable optical parametric generation in a photonic-crystal fiber. *Journal of the Optical Society of America B*, 22(11):2505, November 2005.
- [43] J. Fulconis, O. Alibart, W. J. Wadsworth, P. St.J. Russell, and J. G. Rarity. High brightness single mode source of correlated photon pairs using a photonic crystal fiber. *Optics Express*, 13(19):7572, September 2005.
- [44] M. Azhar, G. K. L. Wong, W. Chang, N. Y. Joly, and P. St.J. Russell. Raman-free nonlinear optical effects in high pressure gas-filled hollow core pcf. *Optics Express*, 21(4):4405, February 2013.
- [45] T. Balciunas, C. Fourcade-Dutin, G. Fan, T. Witting, A. A. Voronin, A. M. Zheltikov, F. Gerome, G. G. Paulus, A. Baltuska, and F. Benabid. A strong-field driver in the single-cycle regime based on self-compression in a kagome fibre. *Nature Communications*, 6(1):6117, January 2015.
- [46] M. Huang, D. Wu, H. Ren, L. Shen, T. W. Hawkins, J. Ballato, U. J. Gibson, M. Beresna, R. Slavík, J. E. Sipe, M. Liscidini, and A. C. Peacock. Classical imaging with undetected photons using four-wave mixing in silicon core fibers. *Photonics Research*, 11(2):137, January 2023.
- [47] Shuai Dong, Xin Yao, Wei Zhang, Sijing Chen, Weijun Zhang, Lixing You, Zhen Wang, and Yidong Huang. True single-photon stimulated four-wave mixing. *ACS Photonics*, 4(4):746–753, March 2017.

Exploring the role of polarization in fiber-based quantum sources: supplemental document

1 Classical field energy

The classical electromagnetic field energy in an optical fiber (or general nonmagnetic dielectrics) reads

$$\mathcal{E} = \frac{1}{2} \int_V d^3\mathbf{r} \left[\frac{d}{d\omega} (\epsilon\epsilon_0\omega) \mathbf{E}^2 + \frac{1}{\mu_0} \mathbf{B}^2 \right], \quad (1)$$

where the integration runs over the full quantization volume which extends over the fiber length L in z -direction and over the complete infinite plane in x - and y - direction,

$$V = (-\infty, \infty) \times (-\infty, \infty) \times [0, L]. \quad (2)$$

Integration by parts yields

$$\begin{aligned} \int_V d^3\mathbf{r} \mathbf{B}^2 &= \int_V d^3\mathbf{r} (\nabla \times \mathbf{A}) \cdot (\nabla \times \mathbf{A}) \\ &= - \oint_{\partial V} ((\nabla \times \mathbf{A}) \times \mathbf{A}) \cdot dS + \int_V d^3\mathbf{r} (\nabla \times (\nabla \times \mathbf{A})) \cdot \mathbf{A}. \end{aligned} \quad (3)$$

The surface terms becomes zero with appropriately chosen boundary conditions. The second term can be evaluated using

$$\begin{aligned} \nabla \times (\nabla \times \mathbf{A}) &= \alpha (\nabla \times (\nabla \times \mathbf{f})) + \alpha^* (\nabla \times (\nabla \times \mathbf{f}^*)) \\ &= \alpha \frac{\epsilon\omega^2}{c^2} \mathbf{f} + \alpha^* \frac{\epsilon\omega^2}{c^2} \mathbf{f}^* \\ &= \omega^2 \mu_0 \epsilon_0 \epsilon (\alpha \mathbf{f} + \alpha^* \mathbf{f}^*), \end{aligned} \quad (4)$$

therefore,

$$\begin{aligned} [\nabla \times (\nabla \times \mathbf{A})] \cdot \mathbf{A} &= \omega^2 \mu_0 \epsilon_0 \epsilon (\alpha \mathbf{f} + \alpha^* \mathbf{f}^*) \cdot (\alpha \mathbf{f} + \alpha^* \mathbf{f}^*) \\ &= \omega^2 \mu_0 \epsilon_0 \epsilon (\alpha^2 \mathbf{f}^2 + \alpha^{*2} \mathbf{f}^{*2} + 2\alpha\alpha^* \mathbf{f} \cdot \mathbf{f}^*). \end{aligned} \quad (5)$$

In an optical fiber, the mode profiles $\mathbf{f}^{(*)}(\mathbf{r})$ vary as $e^{\pm i\beta z}$, hence, upon integration over the full fiber length L ,

$$\begin{aligned} \int_V d^3\mathbf{r} \mathbf{B}^2 &= \int_V d^3\mathbf{r} (\nabla \times (\nabla \times \mathbf{A})) \cdot \mathbf{A} \\ &= \int_V d^3\mathbf{r} 2\omega^2 \mu_0 \epsilon_0 \epsilon(\mathbf{r}) \alpha \alpha^* \mathbf{f} \cdot \mathbf{f}^*. \end{aligned} \quad (6)$$

Furthermore,

$$\begin{aligned} \int_V d^3\mathbf{r} \mathbf{E}^2 &= - \int_V d^3\mathbf{r} \omega^2 (\alpha \mathbf{f} - \alpha^* \mathbf{f}^*)^2 \\ &= - \int_V d^3\mathbf{r} \omega^2 (\alpha^2 \mathbf{f}^2 + \alpha^{*2} \mathbf{f}^{*2} - 2\alpha\alpha^* \mathbf{f} \cdot \mathbf{f}^*) \\ &= \int_V d^3\mathbf{r} 2\omega^2 \alpha \alpha^* \mathbf{f} \cdot \mathbf{f}^*, \end{aligned} \quad (7)$$

again using the $e^{\pm i\beta z}$ dependence of \mathbf{f} . Thus, the complete expression for the classical field energy is

$$\begin{aligned}
\mathcal{E} &= \frac{1}{2} \int_V d^3\mathbf{r} \left[\frac{d}{d\omega} (\epsilon\epsilon_0\omega) \mathbf{E}^2 + \frac{1}{\mu_0} \mathbf{B}^2 \right] \\
&= \frac{1}{2} \int_V d^3\mathbf{r} \left[\frac{d}{d\omega} (\epsilon\epsilon_0\omega) (2\omega^2 \alpha \alpha^* \mathbf{f} \cdot \mathbf{f}^*) + \frac{1}{\mu_0} (2\omega^2 \mu_0 \epsilon_0 \epsilon(\mathbf{r}) \alpha \alpha^* \mathbf{f} \cdot \mathbf{f}^*) \right] \\
&= \omega^2 |\alpha^2| \int_V d^3\mathbf{r} \left[\left(\frac{d}{d\omega} (\epsilon\epsilon_0\omega) + \epsilon\epsilon_0 \right) |\mathbf{f}|^2 \right] \\
&= 2\omega^2 |\alpha^2| \int_V d^3\mathbf{r} \left[\frac{\frac{d}{d\omega} (\epsilon\omega) + \epsilon}{2} \epsilon_0 |\mathbf{f}|^2 \right].
\end{aligned} \tag{8}$$

2 Triplet generation Interaction Hamiltonian

$$\begin{aligned}
\hat{H}_I &= -24\epsilon_0 \chi_{ijkl}^{(3)} \int_{V_I} d^3\mathbf{r} \left(i \sqrt{\frac{\hbar\omega_p}{2}} a_p f_{p,i}(\mathbf{r}) \right) \\
&\quad \left(-i \sqrt{\frac{\hbar\omega_{s_1}}{2}} a_{s_1}^\dagger f_{s_1,j}^*(\mathbf{r}) \right) \left(-i \sqrt{\frac{\hbar\omega_{s_2}}{2}} a_{s_2}^\dagger f_{s_2,k}^*(\mathbf{r}) \right) \left(-i \sqrt{\frac{\hbar\omega_{s_3}}{2}} a_{s_3}^\dagger f_{s_3,l}^*(\mathbf{r}) \right) + h.c. \\
&= 24 \chi_{ijkl}^{(3)} \epsilon_0 \sqrt{\frac{\hbar\omega_p}{2}} \sqrt{\frac{\hbar\omega_{s_1}}{2}} \sqrt{\frac{\hbar\omega_{s_2}}{2}} \sqrt{\frac{\hbar\omega_{s_3}}{2}} a_p a_{s_1}^\dagger a_{s_2}^\dagger a_{s_3}^\dagger \frac{1}{L^2} \frac{1}{\sqrt{M_p M_{s_1} M_{s_2} M_{s_3}}} \\
&\quad \int_{L_I} dz e^{i(\beta_p - \beta_{s_1} - \beta_{s_2} - \beta_{s_3})z} \int_{A_I} dx dy e_{p,i}(x,y) e_{s_1,j}^*(x,y) e_{s_2,k}^*(x,y) e_{s_3,l}^*(x,y) + h.c. \\
&= 24 \chi_{ijkl}^{(3)} \epsilon_0 \sqrt{\frac{\hbar\omega_p}{2}} \sqrt{\frac{\hbar\omega_{s_1}}{2}} \sqrt{\frac{\hbar\omega_{s_2}}{2}} \sqrt{\frac{\hbar\omega_{s_3}}{2}} a_p a_{s_1}^\dagger a_{s_2}^\dagger a_{s_3}^\dagger \frac{1}{L^2} \frac{1}{\sqrt{M_p M_{s_1} M_{s_2} M_{s_3}}} \\
&\quad \int_{L_I} dz e^{i(\beta_p - \beta_{s_1} - \beta_{s_2} - \beta_{s_3})z} \int_{A_I} dx dy \mathcal{I}_{ijkl}(x,y) + h.c.
\end{aligned} \tag{9}$$

3 $\langle \alpha(N_p - 1) | a_p | \alpha(N_p) \rangle$ in the limit of large photon numbers

In order to evaluate the triplet generation rate, the approximation

$$\begin{aligned}
\langle \alpha(N_p - 1) | a_p | \alpha(N_p) \rangle &= \left(e^{-\frac{N_p-1}{2}} \sum_{m=0}^{\infty} \frac{(N_p-1)^{\frac{m}{2}}}{(m!)^{\frac{1}{2}}} \langle m | p \rangle \right) a_p \left(e^{-\frac{N_p}{2}} \sum_{n=0}^{\infty} \frac{N_p^{\frac{n}{2}}}{(n!)^{\frac{1}{2}}} |n\rangle_p \right) \\
&= e^{-\frac{N_p-1}{2}} e^{-\frac{N_p}{2}} \left(\sum_{m=0}^{\infty} \frac{(N_p-1)^{\frac{m}{2}}}{(m!)^{\frac{1}{2}}} \langle m | p \rangle \right) \left(\sum_{n=1}^{\infty} \frac{N_p^{\frac{n}{2}}}{(n!)^{\frac{1}{2}}} \sqrt{n} |n-1\rangle_p \right) \\
&= e^{-\frac{N_p-1}{2}} e^{-\frac{N_p}{2}} \left(\sum_{m=0}^{\infty} \frac{(N_p-1)^{\frac{m}{2}}}{(m!)^{\frac{1}{2}}} \langle m | p \rangle \right) \left(\sum_{n=0}^{\infty} \frac{N_p^{\frac{n+1}{2}}}{(n!)^{\frac{1}{2}}} |n\rangle_p \right) \\
&= \sqrt{N_p} e^{-\frac{N_p-1}{2}} e^{-\frac{N_p}{2}} \left(\sum_{m=0}^{\infty} \frac{(N_p-1)^{\frac{m}{2}}}{(m!)^{\frac{1}{2}}} \right) \left(\sum_{n=0}^{\infty} \frac{N_p^{\frac{n}{2}}}{(n!)^{\frac{1}{2}}} \right) \delta_{mn} \\
&= \sqrt{N_p} e^{-\frac{N_p-1}{2}} e^{-\frac{N_p}{2}} \left(\sum_{n=0}^{\infty} \frac{(\sqrt{(N_p-1)N_p})^n}{n!} \right) \\
&= \sqrt{N_p} e^{-\frac{N_p-1}{2}} e^{-\frac{N_p}{2}} e^{\sqrt{(N_p-1)N_p}} \\
&\approx \sqrt{N_p}
\end{aligned} \tag{10}$$

holds in the limit of large photon numbers since

$$\lim_{N_p \rightarrow \infty} \frac{N_p-1}{2} + \frac{N_p}{2} - \sqrt{(N_p-1)N_p} = 0. \tag{11}$$

4 Mode overlap for triplet generation in a tapered optical fiber: LCP-LCP-LCP triplet configuration

Here we show the mode overlap components in cylindrical coordinates for an LCP pump and triplet generation in the LCP-LCP-LCP configuration.



Figure 1: Real and imaginary parts of all components of the mode overlap integrand \mathcal{I}_{ijkl} for the LCP \rightarrow 3 \times LCP configuration (part 1).

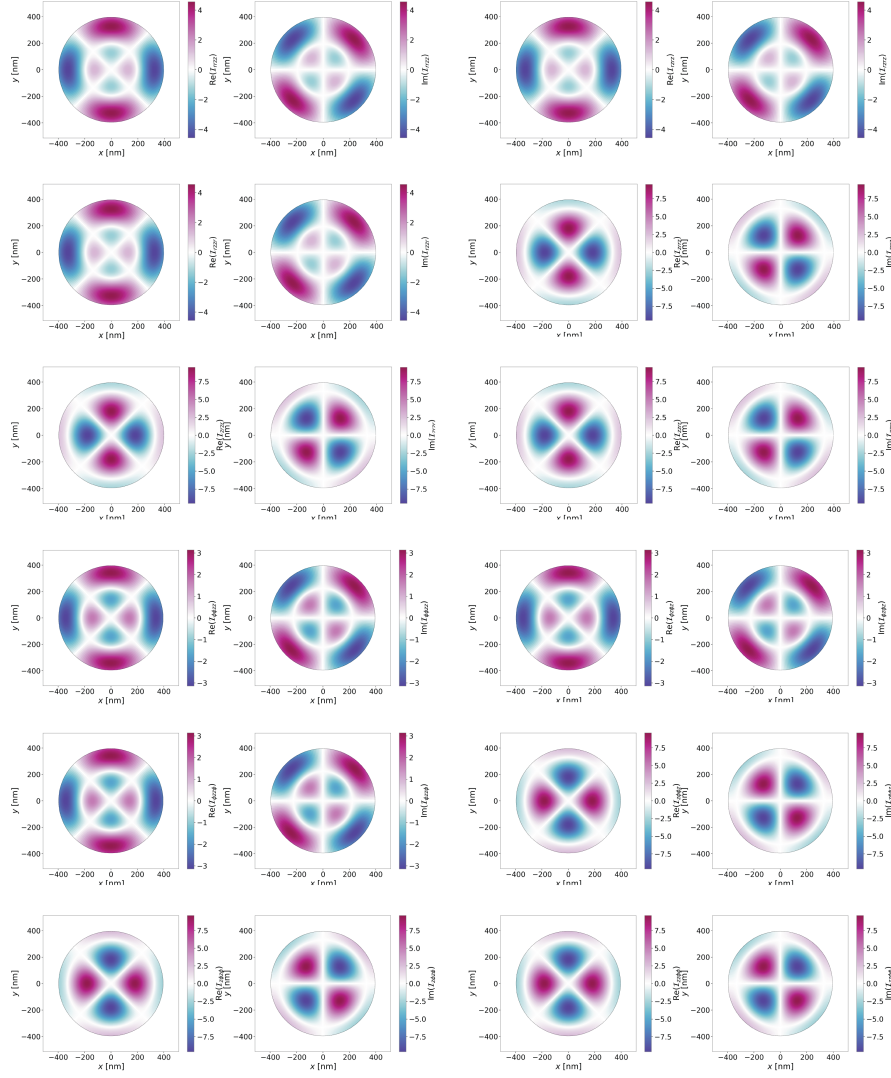


Figure 2: Real and imaginary parts of all components of the mode overlap integrand \mathcal{I}_{ijkl} for the LCP \rightarrow 3 \times LCP configuration (part 2).

5 Mode overlap for triplet generation in a tapered optical fiber: LCP-RCP-RCP, RCP-RCP-RCP triplet configuration

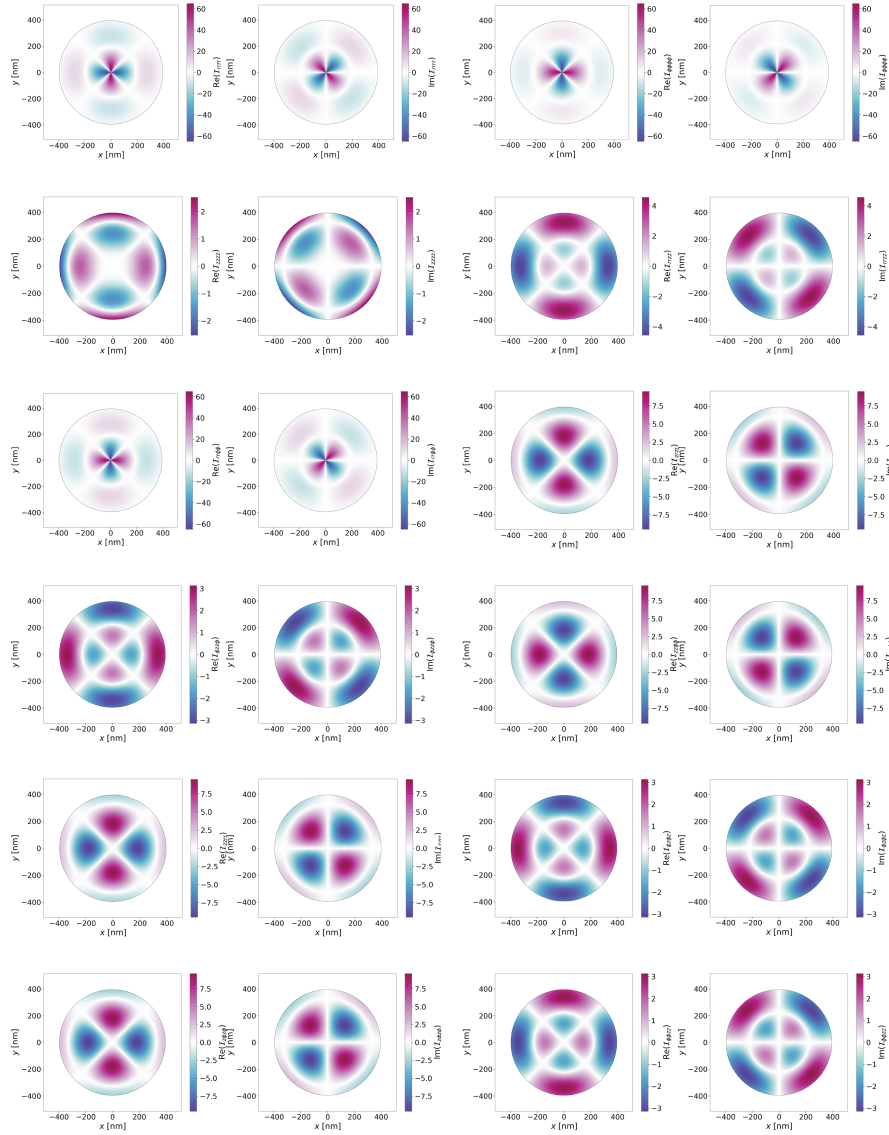


Figure 3: Real and imaginary parts of components of the mode overlap integrand \mathcal{I}_{ijkl} for the LCP \rightarrow 1 \times LCP, 2 \times RCP configuration.

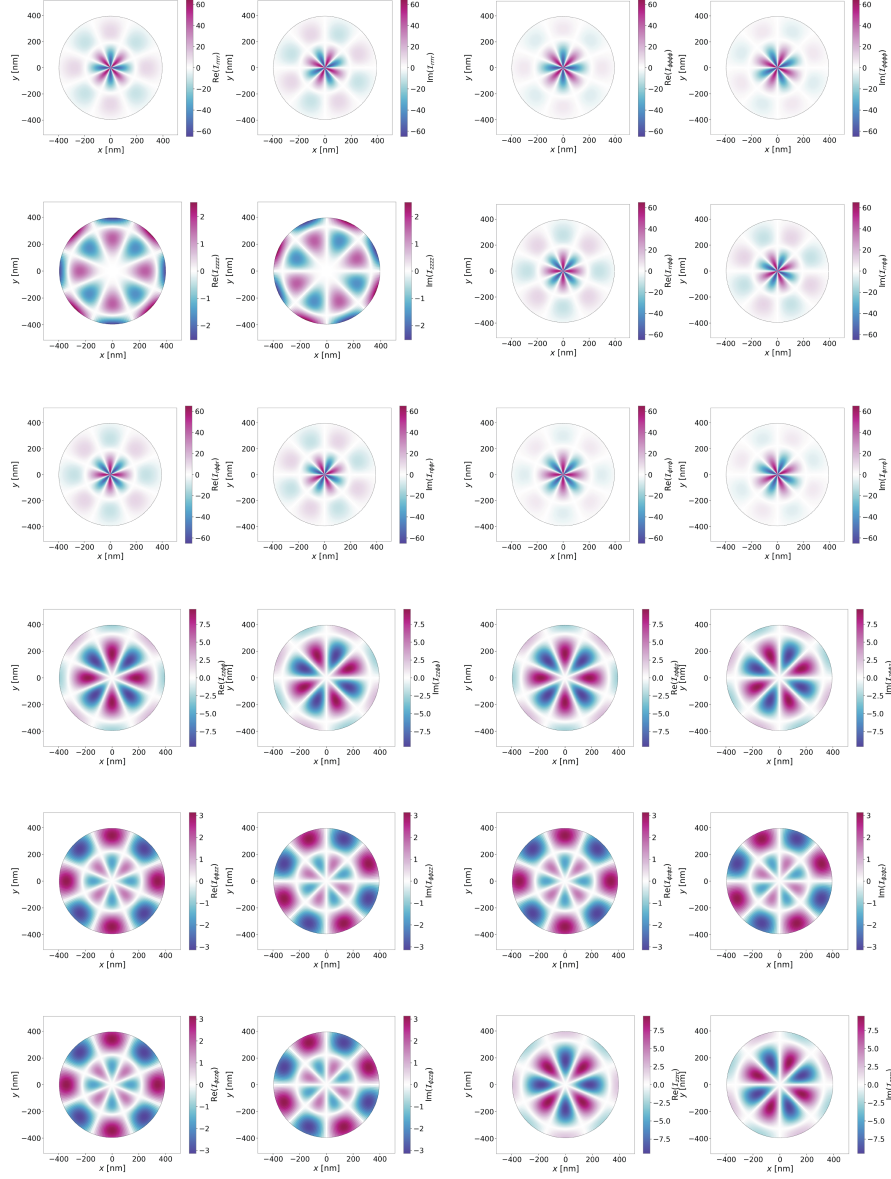


Figure 4: Real and imaginary parts of components of the mode overlap integrand \mathcal{I}_{ijkl} for the LCP \rightarrow 3 \times RCP configuration.